Improving energy efficiency of magnetic CO 2 methanation by modifying coil design, heating agents, and by using eddy currents as the complementary heating source

Stéphane Faure, Sumeet S Kale, Nicolas Mille, Simon Cayez, Thibault Ourlin, Katerina Soulantica, Julian Carrey, Bruno Chaudret

Journal of Applied Physics

Improving energy efficiency of magnetic CO_2 methanation by modifying coil design, heating agents, and by using eddy currents as the complementary heating source

Cite as: J. Appl. Phys. **129**, 044901 (2021); https://doi.org/10.1063/5.0035655
Submitted: 30 October 2020 . Accepted: 07 January 2021 . Published Online: 25 January 2021

Stéphane Faure, Sumeet S. Kale, Nicolas Mille, Simon Cayez, Thibault Ourlin, Katerina Soulantica, Julian Carrey, and Bruno Chaudret

Journal of Applied Physics ARTICLE scitation.org/journal/jap

Improving energy efficiency of magnetic CO_2 methanation by modifying coil design, heating agents, and by using eddy currents as the complementary heating source

Cite as: J. Appl. Phys. **129**, 044901 (2021); doi: 10.1063/5.0035655
Submitted: 30 October 2020 · Accepted: 7 January 2021 ·
Published Online: 25 January 2021

Stéphane Faure,[a] Sumeet S. Kale,[b] Nicolas Mille, Simon Cayez, Thibault Ourlin, Katerina Soulantica, Julian Carrey, and Bruno Chaudret

AFFILIATIONS

Laboratoire de Physique et Chimie des Nano-Objets (LPCNO), Université de Toulouse-INSA-UPS, 135 Avenue de Rangueil, F-31077 Toulouse, France

[a]**Author to whom correspondence should be addressed:** s_faure@insa-toulouse.fr
[b]**Present address:** Institute for Chemical Technology and Polymer Chemistry (ITCP), Karlsruhe Institute of Technology (KIT), Engesserstr. 20, 76131, Karlsruhe, Germany.

ABSTRACT

The Sabatier reaction activated by high-frequency magnetic fields is a promising approach for the power-to-gas process because of expected high energy efficiencies and fast switch-on times. Recent progresses have been achieved by combining nanoparticles displaying both a high heating power and a good catalytic activity. Here, we alternatively use iron microparticles associated with our own-designed Ni/CeO_2 catalyst. The heating agent is cheap and abundant, and we demonstrate that the presence of eddy currents in the system improves its heating performance. The contribution of eddy currents to global heating is successfully determined by an original protocol consisting in comparing a calorimetric and a high-frequency hysteresis loop-based method to measure heating power. In addition, the optimization of the catalyst bed using SiC-spacers limits sintering and thus improves the durability of the catalyst. The energy efficiency of the catalysis process, calculated as a function of coil consumption and gas flow, is clearly improved by the use of an air-cooled Litz wire coil. These improvements are a step forward toward the development of a cheap and efficient process for chemical energy storage.

I. BACKGROUND

The energy transition imposed by the progressing scarcity of resources and anthropogenic climate change requires us to increase the share of renewable energies in the total power mix. Renewable energies are intermittent sources of electricity that, when in excess, are hard to couple with the electric grid infrastructure. Hence, efforts are nowadays devoted to energy storage technologies.

Catalytic conversion of CO_2 to chemicals and fuels represents one of the major approaches for energy storage. Among the different options for transforming CO_2, its hydrogenation into methane seems to be a promising process. Required H_2 is produced through electrolysis using electricity derived from renewable energies. This so-called power-to-gas technology offers a feasible solution in terms of energy storage and integration of renewable energies.[1,2]

Although CO_2 methanation is thermodynamically favorable due to its strong exothermic character (CO_2 (g) + $4H_2$ (g) → CH_4 (g) + $2H_2O$ (g), $\Delta H_{298} = -165.0$ kJ mol^{-1}, $\Delta G_{298} = -113.2$ kJ mol^{-1}), its activation faces significant kinetic limitations. Selecting a high-performance catalyst is the key step to overcome this kinetic limitation and achieve a high CO_2 conversion rate together with a high CH_4 selectivity at low temperatures.[3–5] Ni based catalysts have been the most widely studied due to the best trade-off between activity and cost.[6–8]

Support plays an important role in catalysis by ensuring optimized performance and catalyst stability.[9] In this respect, cerium oxide (CeO_2) is the performant support that promotes CO_2 activation[10–12] for the methanation process. Furthermore, due to its high exothermicity, the CO_2 methanation reaction can lead to the formation of hot spots in the catalyst bed.[13] The real temperature of the catalyst bed is usually much higher than the preset reactor temperature. Therefore, the potential thermal sintering of the Ni metallic active centers is also an important concern for this process.[14,15] It is then necessary to design and synthesize Ni based catalysts with high dispersion and sintering resistance.

CO_2 methanation is industrially performed in continuous flow reactors using conventional heating. An alternative would be magnetic heating, recently applied successfully in heterogeneous catalysis.[16,17] Magnetic catalysis is a concept based on the fact that ferromagnetic materials placed in a high-frequency alternating magnetic field release heat through hysteresis and eddy losses. Hence, by using magnetic materials, the heat is instantly and homogeneously distributed within the catalyst without the need for heating the whole reactor system. Additionally, magnetic heating permits us to reach the target temperature in a few seconds, which makes the system suitable for energy intermittence, a main feature of renewable sources.

Since the first proofs of concept,[18–20] several publications have reported the successful applications of magnetic catalysis to methanation,[21,22] hydrodeoxygenation,[23] and steam and dry reforming.[24,25] However, a few reports address the problem of the energy required by the inductor and the efficient transfer of energy to the chemical reaction.[17,26] Almind *et al.* discussed the influence of the inductor geometry on the power losses and showed an interesting energy transfer efficiency, namely, a 23% transfer of magnetic energy to the chemical reaction, at 90% methane conversion, whereas they predict a 90% efficiency for large-scale production.[26] Despite continuous improvements, experimental results remain up to now well below the theoretical limits. A poor efficiency might be due to several factors. First, cooling the coil requires spending additional energy (approximately 40% of the coil power) when using a chiller or wasting a lot of water if running tap water is used. Second, if reactor filling and heating power of the particles are not optimized, only a small part of the magnetic energy is absorbed by the magnetic material and transformed into heat. A straightforward solution consists in increasing the specific absorption rate (SAR) of the magnetic particles.[17] Indeed, commercial iron oxide particles have generally a small SAR ~10–100 W g^{-1} (Ref. 27), whereas particles with a SAR of over 1000 W g^{-1} have been produced in our laboratory, but they require a sophisticated synthesis and, therefore, remain costly.[17] Third, if the catalyst is not fully optimized, a low methane production reduces the global efficiency of the system. Finally, an additional problem concerns the exact coil geometry: a trade-off must be found between the electric-to-magnetic conversion efficiency (better realized with small size coils) and the limitation of heat loss through reactor walls (better achieved in large coils).[26]

Here, we report a simple and operative process for magnetically induced methane production from CO_2. Special attention has been devoted to the energy efficiency and durability of the process. In order to achieve this goal, we have used cheap commercial iron microparticles as heating agents and a new Ni/CeO_2 catalyst prepared from an organometallic precursor. We show that adding a silicon carbide (SiC) support improves the stability of the catalysts by preventing sintering and favors the formation of eddy currents. In order to determine the contribution of eddy currents to the heating power of iron microparticles, we have used an original protocol, which consists in comparing the heating power values measured by two different methods: a calorimetric one, which gives access to the total heating power, and high-frequency hysteresis loop measurements, which provide the contribution of hysteresis losses only, the difference between the two being the contribution of eddy currents. Finally, an air-cooled Litz wire coil working at relatively low frequency (100 kHz) was used to minimize the energy required to drive the magnetic field, permitting us to improve the energy efficiency of the process.

II. METHODS

Commercial iron (Fe) powder [Sigma-Aldrich ≥99%, reduced, powder (fine)] was used as a heating agent.

A. Synthesis of Ni doped CeO_2

10 wt. % of Ni supported on CeO_2 was prepared by decomposing Ni $(COD)_2$ on the support at 150 °C. Typically, CeO_2 (1 g) was added to a yellow solution of Ni $(COD)_2$ (520.6 mg) in mesitylene (20 ml) in the glovebox. The resulting mixture was sonicated for 20 min and then stirred under argon at room temperature for 30 min. The solution was then refluxed at 150 °C for 1 h under rigorous stirring (700 rpm). At the end of the reaction, the Ni supported on CeO_2 was recovered by decantation of the supernatant solution, washed with THF (5 ml × three times), and dried under vacuum at 100 °C overnight. Ni particles averaged diameter of 5 ± 1 nm was measured by SEM.

B. Preparation of the catalytic bed Fe/Ni/CeO_2/SiC

Several catalysts with a constant amount of Ni/CeO_2 were homogeneously mixed with Fe powder particles (catalyst packing inside the reactor is shown in the inset of Fig. SI 2 in the supplementary material). Two sets of samples Fe/Ni/CeO_2 and Fe/Ni/CeO_2/SiC were prepared. For SiC pellets (Thermo-Fischer coarse, 46 grit) containing samples, the iron mass was fixed to m(Fe) = 2 g and the catalyst mass m(Ni/CeO_2) = 0.45 g. Only the SiC amount was changed.

C. Composition of the catalytic bed

The occurrence of eddy currents and sintering effects is expected to strongly depend on the concentration of iron particles inside the sample. Since the diameter of the particles (Fe, CeO_2, SiC) are very different (see Table I), the mixed powder packing fraction strongly differs from sample to sample, especially for the SiC-containing catalytic beds (see Table II). Analysis of our data has shown that the most relevant quantity to rationalize our results is the Fe volume fraction, which is the volume of iron inside the sample divided by the total volume occupied by the powder

TABLE I. Some physical properties of the magnetic material and the catalyst.

	Average diameter (μm)	Density ρ (g cm^{-3})	Heat capacity Cp (J kg^{-1} K^{-1})
Fe powder	[0.5–5]	7.86	449
CeO_2	[0.05–0.5]	7.22	390
SiC	[325–425+]	3.16	750

(and thus including air), defined as

$$VF(\mathrm{Fe}) = \frac{V_{th}(\mathrm{Fe})}{V_{powder}} = \frac{m_{\mathrm{Fe}}/\rho_{\mathrm{Fe}}}{\pi r^2 h_{catalyst}}, \quad (1)$$

with V_{th}(Fe) being the theoretical iron particle volume calculated from the weighted mass m_{Fe} and the density ρ_{Fe} and V_{powder} being the total volume of powder inside the reactor that is a cylinder here. V_{powder} includes the interparticle voids, and it is thus calculated from the internal radius r of the reactor and the height of catalyst $h_{catalyst}$.

The iron volume fraction was adjusted by mixing pure CeO_2 or an SiC-spacer agent to the Ni/CeO_2 catalyst. The list of the catalysts and their composition is given in Table II. The sample labeled Ce25 (similar to the sample Ce25-2, see Table II) does not contain SiC and is an exception. It is used for comparison.

TABLE II. List of catalysts and their composition used in CO_2 methanation and ICP analyses. The nomenclature of the sample's name is as follows: AX-m(Fe), with A = (Ce or SiC) the bed composition, CeO_2 bed is labeled (Ce) and CeO_2/SiC bed is labeled (SiC). X indicates the iron volume fraction (formula 3), and m(Fe) indicates the iron mass content.

Name	Fe Volume fraction (%)	Wt (Fe) (g)	Wt (Ni/CeO_2) (g)	% Ni/CeO_2	Wt (CeO_2) (g)	Wt (SiC) (g)
SiC spacer-free catalytic bed						
Ce27-3	27	3	0.4		0	…
Ce25-2	24.9	2	0.4		0	…
Ce20-1	20.2	1	0.4		0	…
Ce19-2	19.1	2	0.4		0.4	…
Ce19-3	18.7	3	0.4	9.27	0.93	…
Ce13-2	13.1	2	0.4	9.27	0.9	…
Ce13-3	13.1	3	0.4	9.27	1.6	…
Catalytic bed w/SiC spacer						
Ce25	24.9	2	0.4		0	…
SiC20	20.2	2	0.45		…	0.35
SiC15	14.7	2	0.45		…	1
SiC13	13.3	2	0.45	9.47	…	1.3
SiC13bis	13	2	0.45		…	1.7
SiC9	9.3	2	0.45		…	3

D. SAR measurements

The SAR was measured *in situ* in the reactor used for catalysis with a K-type thermocouple. The protocol for SAR measurements consists in applying a low intensity magnetic field (μ_0H = 18 mT) for 10 min, measuring the temperature rise and deducing SAR from the initial slope. It was deduced from the initial slope $\Delta T/\Delta t$ according to the equation

$$\mathrm{SAR}(W/g) = \frac{\sum_i Cp_i m_i}{m_{\mathrm{Fe}}} \times \frac{\Delta T}{\Delta t}, \quad (2)$$

with Cp_i being the heat capacity and m_i being the mass of the material referred by index i.

E. Magnetically induced catalysis

The continuous flow reactor was designed by our team in collaboration with the Avitec and iBEAM companies (Fig. SI 1 in the supplementary material). The reactor is made of glass (internal diameter 1 cm) and placed inside the coil of an air-cooled inductor delivering an alternating magnetic field oscillating at a frequency of 100 kHz [see Fig. SI 2 in the supplementary material for details on the inductor) and with a 70 W background power consumption (Fig. SI 3 in the supplementary material). The power consumption of the power supply was measured by a POLIER MM32ML series energy meter. The magnetic field intensity $\mu_0 H$ was varied between 0 and 60 mT, and the total flow rate was set to 25 ml min^{-1} throughout the experiment. Gas commercial bottles (H_2, CO_2 with purity >99.9999%) were connected to the setup with remote control gas valves to ensure precise control of the flow.

Catalytic experiments were carried out with a H_2:CO_2 molar ratio of 4:1 under ambient pressure for at least 4 h. The temperature was monitored by a K-type thermocouple positioned inside a glass capillary in contact with the catalytic bed. A blank test was performed to check that perturbations due to the induction field on the temperature measurement are negligible (see the supplementary material).

After the magnetic field was switched on, the temperature inside the reactor increased progressively until the onset of the methanation reaction. Then, the heat released during CO_2 methanation led to an increase in temperature inside the catalyst bed. During catalysis, the coil power was adjusted to maintain the temperature in the range T = 320–350 °C so that, on the one hand, the CH_4 yield/selectivity was maintained at its maximum, and, on the other, the total used power was minimized.

The catalytic tests were performed under two configurations: (i) ascending (up) gas flow with no overpressure risk (fluidized system). A water-trap was connected above the outlet to avoid that water drops on the bed and wet the catalyst. (ii) Descending (down) gas flow, in this case, silicon carbide (SiC) powder spacer was added to the bed mixture. Condensed water formed during the course of the reaction was collected in a water-trap flask, which was connected to the outlet of the reactor. Dry gases were analyzed by a mass spectrometer of type GC-MS in a PerkinElmer Clarus SQ 8 system.

It should be noted that the up-flow configuration is not suitable for the catalysis process. Nevertheless, we used it for convenience and for safety reasons to measure the SAR of particles.

We showed above that it does not affect the efficiency of the catalysis reaction. In the down-flow configuration, for safety reasons, a spacer is mandated to prevent the risk of the reactor blockade.

F. Catalysis activated by external heating

The reaction was also performed inside an oven at ambient pressure with the same glass reactor described above in up-flow direction and using the same reaction conditions, including the gas ratio and flow rate. The temperature was also monitored via a thermocouple inside the oven coupled to a PID regulation system and a K-type thermocouple positioned inside a glass capillary in contact with the catalytic bed.

III. RESULTS AND DISCUSSION

In order to carry out the catalytic reactions activated by magnetic induction, we have designed a glass reactor inside that is placed in the catalytic mixture. This mixture is composed of a heating agent, a catalytic material deposited on a support, and a spacer to avoid blocking of the reactor.

For the heating agent, we have chosen to investigate a simple commercial iron powder. We have previously shown that magnetic nanoparticles deposited on an oxide or carbon support could be efficient nano-heaters and could also act as both heaters and catalysts. The iron powder is expected to display a much lower SAR than the nanoparticles but is much cheaper and could also be heated by eddy currents if an electrical connection is present between the grains.

The catalyst, Ni/CeO_2 (10 wt. %), was prepared by an organometallic chemistry route in order to avoid, in our glass system, the calcination/reduction steps classically carried out for the preparation of heterogeneous catalysts. For this purpose, we decomposed the organometallic precursor, Ni$(COD)_2$, over a suspension of CeO_2, known for displaying good properties for CO_2 activation,[28] in mesitylene at 150 °C. Although a large number of methanation catalysts are known, an additional advantage of this method is that there is no doubt on the nature of the catalyst surface. The Ni content was fixed at 10 wt. % relative to CeO_2, and the decomposition takes place within 1 h at 150 °C yielding Ni particles (5 nm average diameter, see Fig. SI 6 in the supplementary material) evenly distributed over ceria. The Ni content and the homogeneity of the distribution of Ni were assessed by SEM-EDX (Fig. SI 7 in the supplementary material).

The catalytic mixture was prepared by mechanically mixing the iron and the Ni/CeO_2 powders at different relative contents (see Table II). The powder was not compacted. All experiments have been carried out at a flow rate of 25 ml min^{-1}, with a 4:1 ratio of H_2 to CO_2 and a frequency of 100 kHz (standard conditions). The magnetic field was varied between 0 and 60 mT. Catalysis experiments have been performed by injecting the gases from the top of the reactor (down-flow configuration). However, for measuring the heating power of the iron powder in different conditions, gas was injected from the bottom (up-flow configuration) to avoid the clogging of the system.

A. Heating properties of SiC-free catalytic bed

The heating properties of the materials were measured in the standard conditions and an up-flow configuration on different samples containing a mixture of Fe powder and Ni/CeO_2 with a Fe volume fraction between 13% and 25% (see experimental) and a mass of Fe ranging from 1 g to 3 g. The objective of these measurements was to perform screening of the concentrations and masses required to reach a temperature high enough for catalysis. For these measurements, the time evolution of the temperature was recorded for different magnetic field amplitudes. Figure 1(a) shows the maximum temperature reached inside the reactor after 10 min, approximately the time to reach a plateau of temperature, upon

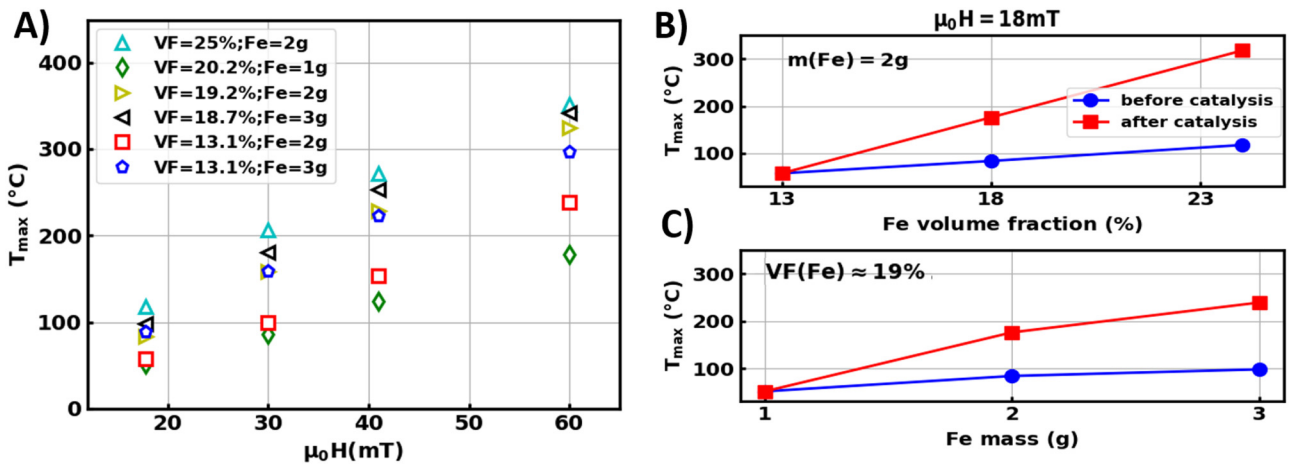

FIG. 1. (a) Maximal temperature reached inside the reactor as a function of the applied magnetic field after 10 min. (Right side) Maximum temperature reached inside the reactor under low magnetic field (18 mT) initially and after performing catalysis for more than 2 h. (b) Different iron volume ratios and constant Fe mass [m(Fe) = 2 g]. (c) Constant iron volume ratio (VF ≈ 19%) and varying Fe masses.

applying a magnetic field between 18 and 60 mT. For more clarity, the data for $\mu_0 H = 18$ mT are shown in Fig. 1(b) (blue circled line) a varying iron volume fraction with a constant iron mass [m(Fe) = 2 g], and Fig. 1(c), a varying iron mass with an approximately constant iron volume fraction (VF ≈ 19%). As expected, the maximum temperature reached inside the reactor increases with the amount of iron and/or the volume fraction. The temperature at which catalysis is expected to occur ($T \geq 300$ °C) can be reached for different volume fractions (13%, 19%, and 25%) by adjusting the amount of iron (3 g, 2–3 g, and 2 g, respectively).

For a constant mass of iron (m(Fe) = 2 g) but increasing Fe volume fraction, the maximum temperature reached slightly increases [see Figs. 1(a) and 1(b)] as a result of the decrease of the total sample volume and therefore of the heat losses of the reactor, leading to higher temperatures. Similarly, when the iron volume ratio is kept constant (VF ≈19%), a slight increase of the maximum temperature reached is observed upon increasing the iron mass [see Figs. 1(a)–1(c)]. Finally, Fig. 1(a) shows that a minimum iron volume fraction is required to reach 300 °C, the necessary temperature to perform catalysis experiments.

The suitable samples have been used for methanation reactions, the result of which will be presented in section V. It can be noted right now that the heating power of the samples evolves after the samples have been submitted for several hours at a magnetic field up to $\mu_0 H = 60$ mT in order to reach the temperature range $T = 320$–350 °C. This effect is illustrated in Figs. 1(b) and 1(c) (red circled lines), which show the maximum temperatures measured under the low magnetic field ($\mu_0 H = 18$ mT) after the samples have been used for catalysis experiments. This evolution is due to structural modifications of the iron support (see below).

B. Heating efficiency of SiC-containing catalytic bed

In order to prevent the clogging of the reactor when carrying out the catalytic reaction with the injection of the gases from the top of the reactor, a third component was added to the iron powder/Ni-CeO_2 mixture, namely, SiC spheres displaying a diameter between 325 μm and 425 μm. The SAR of fresh samples of Fe/SiC/Ni/CeO_2 samples was measured in the standard conditions and after several hours of catalysis, once the reactor was cooled down to room temperature (see experimental). We applied in each case a low power magnetic field ($\mu_0 H = 18$ mT) in order to avoid degradation of the sample due to sintering.

Figure 2 shows the SAR evolution of SiC-containing beds (circle marks), initially (full lines) and after catalysis experiments (dotted lines) for different Fe volume fractions ranging from 9% to 25%. All samples have the same iron content m(Fe) = 2 g. For the sake of comparison, the SAR of the beds containing only CeO_2 (diamond marks) is also presented. The corresponding sample volumes are shown on the top panel for information. SAR values of samples before exposition to the magnetic field are extremely low (<1 W/g) compared to typical values of magnetic nanoparticles. The SAR varies weakly with the Fe volume fraction and type of samples and is slightly lower in the absence of SiC. In contrast, all samples, except those displaying a low Fe volume fraction, show their SAR increased after exposure to the magnetic field, up to 3.5 W g^{-1} in the case of sample SiC20 (see Table II). The SAR of

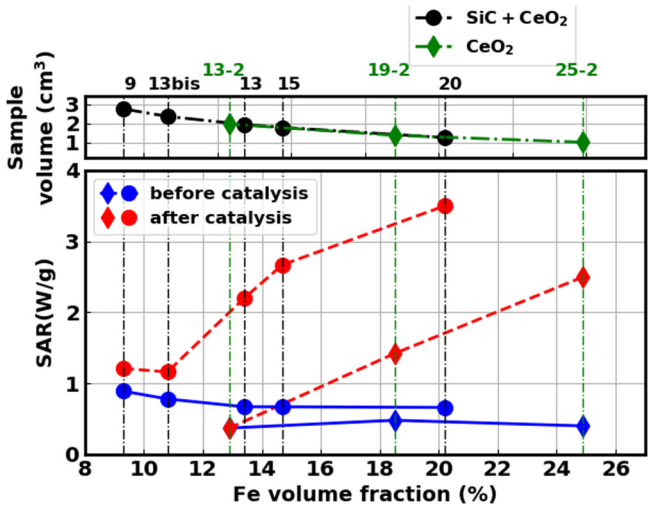

FIG. 2. SAR of samples Ce13-2, Ce19-2, and Ce25-2 (diamond marks) and SiC-containing samples SiC9, SiC13bis, SiC13, SiC15, and SiC20 (circle marks) as a function of the Fe volume fraction (bottom label; for the description of samples, see experimental section Table II). The iron mass is constant m(Fe) = 2 g. The SAR is measured in both cases initially (full lines) and after catalytic experiments (dotted lines). The applied field is $\mu_0 H = 18$ mT. The top panel shows the volume of SiC-free (green diamonds) and SiC-containing samples (black circles). Top labels and vertical dotted lines are a guide for the eyes to identify the samples.

SiC-containing beads increases more and/or at a lower Fe volume fraction than the ones not containing SiC. As a consequence, the presence of SiC-spacer in the powder composition permits us to reach the temperature for catalysis activation with a lower iron volume fraction. This effect will be discussed in Sec. IV.

C. Structural evolution of the samples

We investigated the structural evolution of the catalyst and heating agent after long-time exposure to the magnetic field in standard catalysis conditions, the magnetic field being adjusted to keep the temperature in the range T = 320 °C–350 °C, in the absence and in the presence of the SiC-spacer. Structural evolutions are a well-known side-effect of high temperatures, leading to sintering and shortening the catalyst lifetime.

1. SiC-free samples

In order to avoid clogging of the system, these experiments were carried out in the up-flow configuration. SEM images of the highest volume ratio sample (Ce25-2, VF = 25%; Table II), performed initially and after magnetic heating show that the powder evolved structurally from separated particles before catalysis [Fig. SI 4(a) in the supplementary material] to a dense block after long-time exposure to the magnetic field [Fig. SI 4(b) in the supplementary material]. For samples with a low volume fraction, the agglomeration effect was less pronounced and the resulting blocks were more brittle.

The comparison of XRD analysis of unused pure iron powder with samples Ce13–3 (VF = 13%) and Ce25-2 after magnetic heating [Fig. SI(5) in the supplementary material] clearly evidences structural differences. The sample containing 13.1% iron volume fraction is still mainly composed of Fe(0), whereas in the high (25%) volume fraction sample, Fe_2O_3 or Fe_3O_4 phases are also present as a result of increased water. Oxidation is a sideway effect of catalysis when water is not properly evacuated and depends on the duration during which water molecules stay in contact with iron particles. We observe that, independently of the catalytic bed composition, the sample with 25% iron volume ratio (Ce25-2) is more oxidized that the 13% one (CE13-3 and SiC13), which could originate from the fact that the probability of water to react with iron particles increases as well. Another hypothesis could be that catalysis occurs on a thin layer of the catalytic bed so the produced water oxidizes the iron particles located after the "catalytic layer," the thickness of which could be different in the various samples.

We also verified that the up/down-flow configuration has no influence on the sample evolution independently of its composition, and characterized the Ce25 (VF = 25%) SiC-free sample after catalysis experiments in down-flow configuration. The sample evolution was similar in both up-flow and down-flow configuration. For example, EDX mapping of the Fe/Ni/CeO_2 powders (Ce25-2) in the down-flow configuration before (Fig. SI 7 in the supplementary material) and after (Fig. SI 8 in the supplementary material) catalysis confirms the formation of iron aggregates on a large scale.

2. SiC-containing samples

In this case, all the experiments were carried out in the down-flow configuration. A comparison of SEM observation and EDX mapping of sample SiC13 before (Fig. SI 9 in the supplementary material) and after (Fig. SI 10 in the supplementary material) catalysis evidences a structural evolution of the Fe microparticles: initially the latter are homogeneously mixed with the support; after catalysis, long chains of particles are observed. The two different sample evolutions after exposure to the magnetic field are presented in Fig. 3. The isotropic aggregates observed for the SiC-free sample [Fig. 3(a)] contrast with the chains observed in sample SiC13, Fig. 3(b).

The XRD patterns of unused Fe/Ni/CeO_2/SiC powder with iron volume fraction VF = 13.3% (sample SiC13) as well as pure iron powder are reported in Fig. SI 11 in the supplementary material. The peaks corresponding to the Fe phase are easily identified. The other peaks correspond to the CeO_2 phase. Ni particle concentration is too low to be detected and SiC is amorphous. The presence of iron oxide phases after catalysis is visible on the x-ray diffractogram but in smaller proportions than in the absence of SiC.

In conclusion, all samples undergo a structural evolution independently of the presence or absence of a SiC-spacer. However, the presence of SiC spacer inside the catalytic bed triggers different mechanisms of diffusion and coalescence of iron particles, which will be discussed in Sec. IV.

D. Eddy currents contribution to the total heating

To quantify more precisely the sources of heating power in the samples and explain the SAR evolution, we studied in depth two representative samples (Ce25–2 and SiC13) before and after catalysis. Despite different volume fractions (25% and 13%, respectively), the two samples undergo a similar evolution of their SAR before and after catalysis (see Fig. 2). However, sample SiC13 does not transform into a block, whereas sample Ce25–2 does.

1. Hysteresis and eddy currents contributions to the SAR

We measured the SAR of samples Ce25-2 and SiC13 (see Table II) using two different methods (Fig. 4). The powder was deposited inside a capillary, which was used for both experiments.

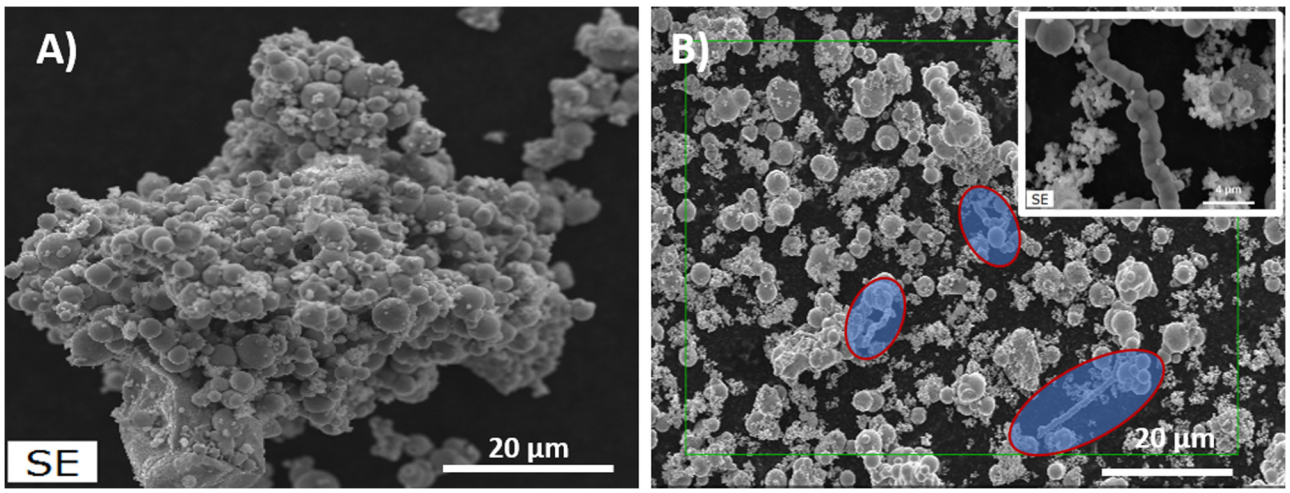

FIG. 3. SEM image after magnetic field exposure in the standard conditions: (a) Fe/Ni/CeO_2 catalyst (sample Ce25-2, *VF* = 25%) and (b) Fe/Ni/CeO_2/SiC catalyst (sample SiC13). The inset shows a zoom in on a chain from a different location in the sample.

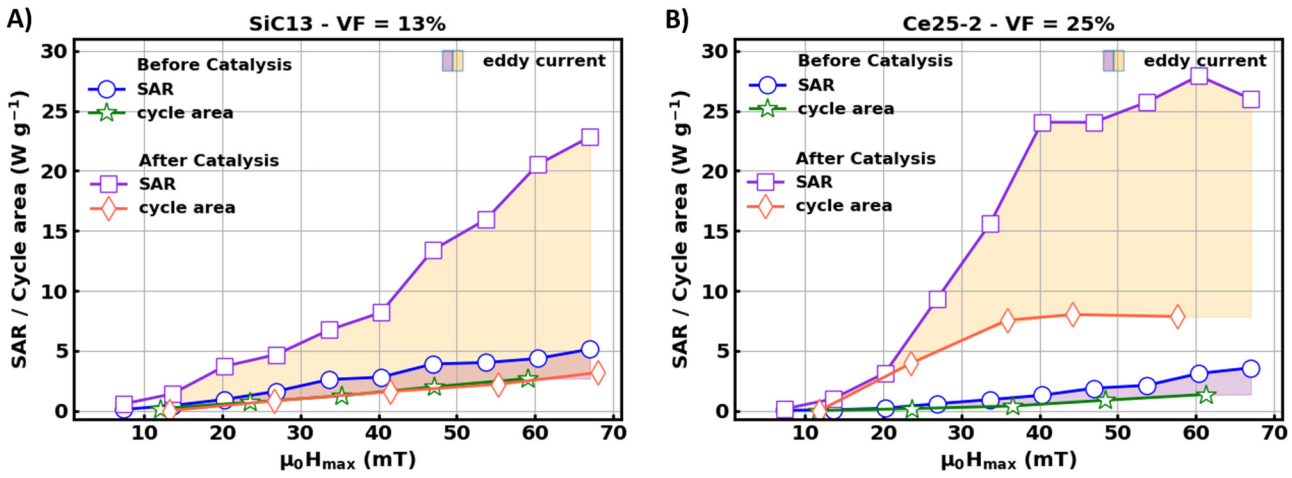

FIG. 4. Energy dissipated upon magnetic field application measured by calorimetric method (labeled "SAR," circle and square line) at 100 kHz and hysteresis cycles (star and diamond line) labeled cycle area) measured at 50 kHz for the sample (a) SiC13 and (b) Ce25-2 before (circle and star line) and after catalysis (square and diamond line). Yellow and red shaded area shows the contribution of eddy current to the total heating.

The first one (blue circle plain lines) is a calorimetric SAR measurement performed in a 100 kHz coil. In these measurements, in contrast to measurements shown in Fig. 2, the samples were not submitted to a gas flow, which removes heat from the sample and leads to underestimate the SAR.[29] The measured SAR values (SAR_{calo}) are 1.5 to 2.5 times higher than the ones obtained in Fig. 2. Initially, SAR_{calo} varies linearly with the magnetic field and is slightly higher for sample SiC13 [Fig. 4(a)] than for sample Ce25–2 [Fig. 4(b)]. After catalysis (blue circle dashed lines), SAR_{calo} is much larger, which confirms the trend already observed in Fig. 2.

The second method is based on the integration of high-frequency hysteresis loops, and only measures the contribution due to hysteresis losses. Details on the experimental setup are given in Ref. 30 The measured hysteresis loops are shown in Fig. 5 for the two samples. These measurements lead to a second heating power value (green stars and orange diamond in Fig. 4). $SAR_{hyst} = A^*f$, where A is the hysteresis area and f the frequency of the magnetic field (50.3 kHz). SAR_{hyst} and SAR_{calo} were both normalized to 100 kHz to be comparable. It means to multiply the $SAR_{hyst} = A^*f$ (where $f = 50$ kHz in our hysteresis loop measurement setup) by a factor 2 to obtain the SAR at 100 kHz. In all circumstances, SAR_{calo} is larger than SAR_{hyst} because the former includes both the heat generated by hysteresis losses and the eddy currents. Hence, the difference (SAR_{calo} - SAR_{hyst}) gives a quantitative measurement of the power dissipated by eddy currents (illustrated as yellow and red shaded areas in Fig. 4). The difference, if any, is very small before exposure to the magnetic field. In sample SiC13, after catalysis, SAR_{hyst} remains unchanged whereas SAR_{calo} increases strongly, evidencing a large contribution of eddy currents to the total heating [yellow shaded area in Fig. 4(a)]. In sample Ce25-2, both SAR_{hyst} and SAR_{calo} increase, showing an approximately similar contribution of eddy currents and hysteresis losses to the total heating [see Fig. 4(b)].

2. Decrease of the magnetic susceptibility induced by eddy currents

The analysis above indicates that, after catalysis, the measured high-frequency hysteresis loops should be significantly affected by the contributions of eddy currents. To our knowledge, this is the first time that high-frequency hysteresis loop measurements are performed on samples displaying both hysteresis losses and eddy currents. It, therefore, justifies a more precise analysis of the hysteresis loops shown in Fig. 5. Sample SiC13 displays clearly a decrease in its magnetic susceptibility after catalysis. To illustrate it, its maximum magnetization is plotted as a function of the applied magnetic field in Fig. 6 (circles). We interpret this feature as resulting from the Lenz's law, i.e., the appearance of electric currents inside the sample creating a magnetic field opposed to the external magnetic field, hence reducing the magnetic signal detected by our pick-up coil. In the case of sample Ce25-2, after catalysis, unusual hysteresis loops are also observed. It should be noted that, usually, hysteresis loops– also called minor cycles – are imbricated one into each other, like Russian dolls, as a function of magnetic field amplitude.[29] Moreover, the susceptibility is supposed to be either constant with the field or to increase with it when particles form chains.[23] Here, hysteresis loops are not imbricated and the susceptibility decreases when increasing the field. We interpret these unusual features as resulting from a diamagnetic response of the sample at large field due to eddy currents. They are thus in agreement with Fig. 4(b), where the strong presence of eddy currents at large field is illustrated.

The iron microparticle oxidation cannot convincingly explain the unusual magnetic properties described in Figs. 4–6. First, oxidation is observed on both samples SiC13 and Ce25-2, whereas magnetization shows opposite behavior (a decrease and an increase, respectively). The less oxidized sample (SiC13) shows a strong decrease of magnetization M_{max}, whereas the strongly oxidized one

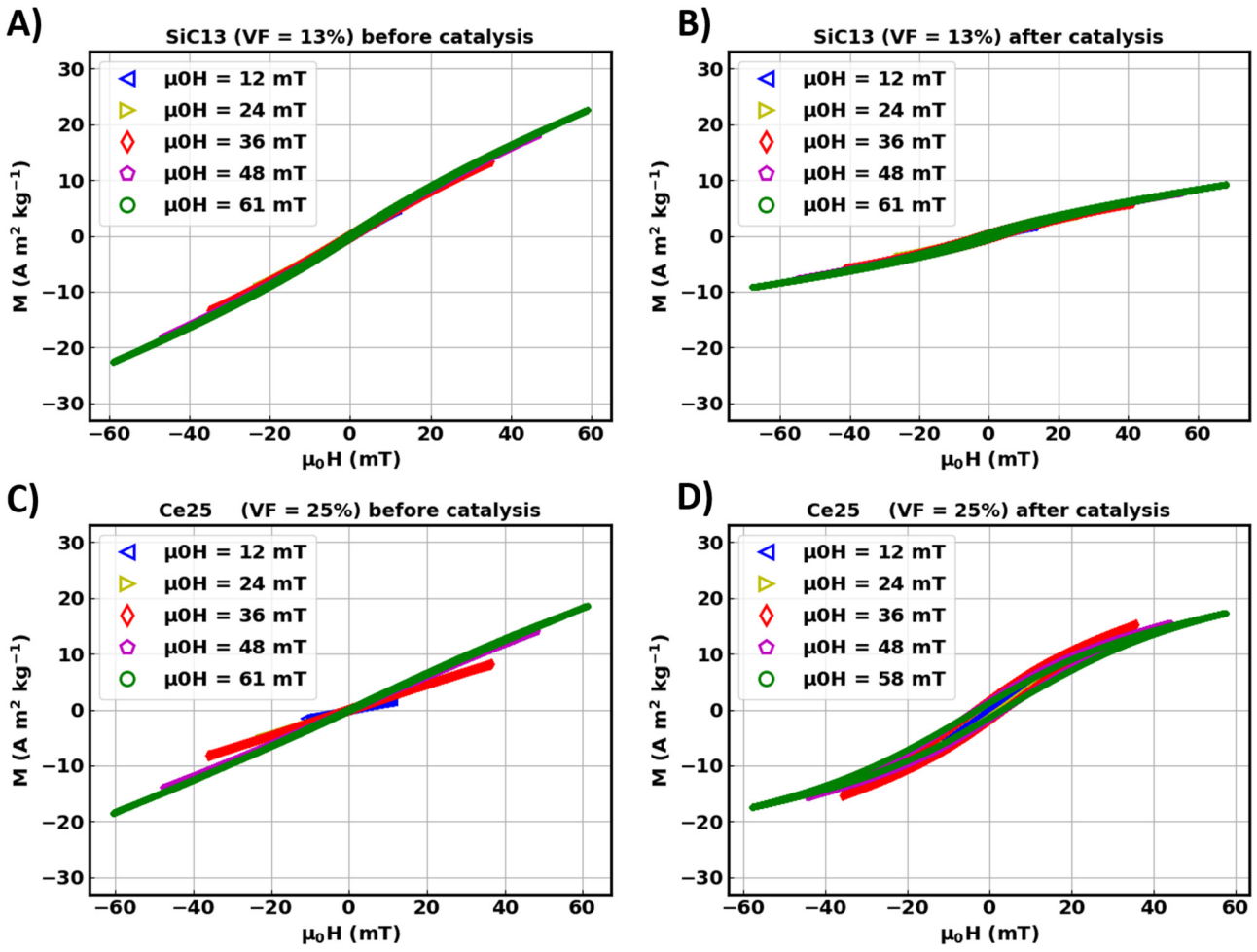

FIG. 5. Hysteresis cycles at room temperature and 50.33 kHz. Sample SiC13 (a) initially and (b) after catalysis. Sample Ce25 (c) initially and (d) after catalysis.

shows an increase of its magnetization (see Fig. 6). Also, it is important to notice that hysteresis loops are minor cycles and then, one cannot conclude on the value of the saturation magnetization (M_s) from the value of the maximum magnetization (M_{max}) extracted from the minor loops.

That is why we privileged the role of structural evolution (due to sintering) on magnetic properties.

IV. DISCUSSION ON THE MECHANISMS UNDERLYING THE HEATING

Figure 7 schematically summarizes the proposed structural evolution of the samples that can explain the different behaviors of the catalysts with and without SiC. In the absence of SiC spacer (Fig. 7, top part), similar size of Fe and CeO_2 particles leads to the agglomeration of iron particles. In this case, the larger susceptibility of the aggregates compared to that of isolated particles leads to increased hysteresis losses. In the presence of SiC particles which are larger than the Fe and CeO_2 ones (Fig. 7, bottom part), the size difference leads to a non-uniform spatial distribution of the particles. When the temperature increases, the smaller particles (Fe and CeO_2) migrate into the interstices created by the larger ones (SiC). As a result, some regions of the bulk are enriched in smaller particles while others are enriched in large particles. This specific mechanism leads to the formation of a microporous network constituted of coalesced iron pellets. Here, the eddy current contribution to the SAR dominates.

Finally, the presence of eddy currents seems very clear in the two samples after catalysis. The presence of SiC particles favors the formation of columns resulting from the coalescence of particles into the large pores of the SiC structure whereas a coalescence of particles into large blocks is observed in the absence of SiC.

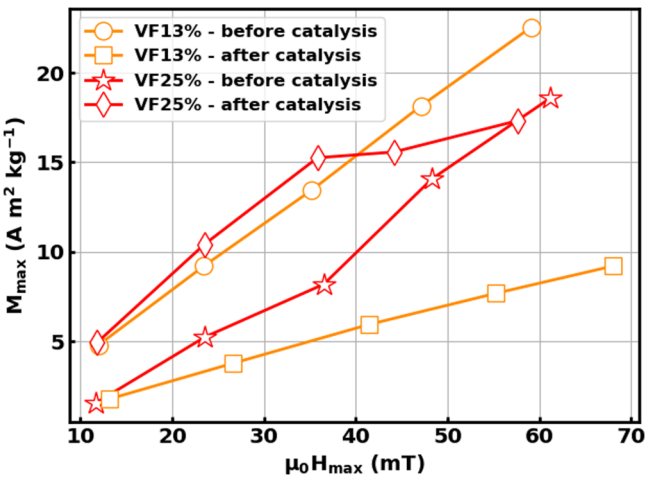

FIG. 6. Maximum magnetization extracted from the minor hysteresis cycle measurements at room temperature and 50 kHz for samples SiC13 and Ce25-2 in function of the applied magnetic field initially (circles and stars, respectively) and after catalysis (square and diamonds, respectively).

V. CATALYSIS PERFORMANCE

A. CO_2 methanation in the absence of SiC spacer

We studied the influence of the sample composition on the stability and performance of the catalyst. For safety reasons, these experiments were performed in the up-flow configuration, because the formation of blocks by sintering (see Sec. III C 1) may lead to dangerous overpressures in the reactor. Figure 8 shows the catalytic performance, namely, the evolution of the carbon dioxide conversion X(CO_2), of the methane yield Y(CH_4) and of the selectivity for methane S(CH_4) as a function of time after an initial delay of 45 min. On the left column of Fig. 8(a), C, E, all catalysts contain the same amount of iron [m(Fe) = 3 g] and the iron volume fraction decreases from 27% [Fig. 8(a)] to 13.1% [Fig. 8(e)]. On the right column, the iron mass is fixed to m(Fe) = 2 g and the volume fraction is 25% [Fig. 8(b)] and 18.5% [Fig. 8(d)]. The steady state regime takes longer to be established as the Fe volume fraction decreases [Figs. 8(d) and 8(e)]. Moreover, for these samples, the minimum magnetic field intensity necessary to activate and maintain the temperature inside the reactor is higher, hence consuming more energy and reducing the overall energy efficiency (see below).

We also note that, during the first hours, CH_4 selectivity is very close to 100 mol. % for all samples, with no traces of CO being detected. However, CH_4 yield starts to decrease for high Fe volume fraction and high iron mass [Figs. 8(a)–8(c)]. This decrease is due to a partial loss of catalytic active sites as a result of sintering of the catalyst and, additionally, to the presence of condensed water because of the geometry of the reactor.

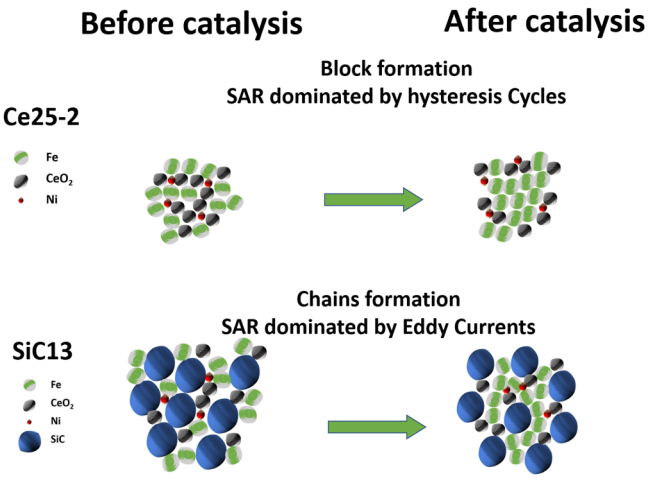

FIG. 7. Scheme that illustrates the difference of evolution between the sample SiC13 and Ce25-2. In the absence of SiC particles (sample Ce25-2), there is a strong aggregation/sintering of iron particles so the SAR is dominated by hysteresis losses. In the presence of SiC particles (sample SiC13), sintering is partial and lead to the formation of a Fe network. The contribution of eddy currents to the SAR dominates.

B. CO_2 methanation performance with SiC-spacer catalyst

Experiments on these samples were performed in the classical top-down configuration using a water condenser after the reactor. An analysis of the catalytic performance of samples displaying different Fe volume fraction (13.3%, 14.7%, and 20%; samples SiC13, SiC15, and SiC20, respectively) show similar selectivity and yield as in SiC-free catalyst (see Fig. 9). The required magnetic field intensity to maintain the catalytic bed temperature increases with decreasing volume fraction. However, the CH_4 selectivity and yield remain constant (100%) all along the experiments, showing that the Ni catalyst remains stable with no activity losses. Complementary experiments show that the sample SiC13 remains stable (no sample evolution) with no loss of CH_4 yield over 15 h activity (see Fig. SI 10 in the supplementary material).

C. Comparison of magnetic and conventional heating

In order to evaluate the possible advantage of magnetic activation of catalysis, we compared a 0.4 g Ni/CeO_2 catalyst (similar to sample Ce27-3, Ce25-2 and Ce20-1, but without iron powder) with external heating provided by an oven. Figure 10 shows that increasing the temperature from 250 °C to 450 °C leads to an increase in CH_4 yield. The maximum CO_2 conversion is observed at 330 °C with almost 99% selectivity to CH_4 (see Fig. 10). Further increase in temperature to 450 °C has no influence on catalytic activity. However, reducing temperature back to 400 °C leads to a slight decrease in CO_2 conversion.

This experiment shows that catalytic results obtained using magnetic heating and conventional heating are more or less comparable. However, the use of magnetic heating has the advantage of activating the reaction within a few minutes (working temperature is reached in 10 min for high volume fraction samples under magnetic field against more than 1 h in the oven). Moreover, we have shown here that it is possible to work at a low magnetic field

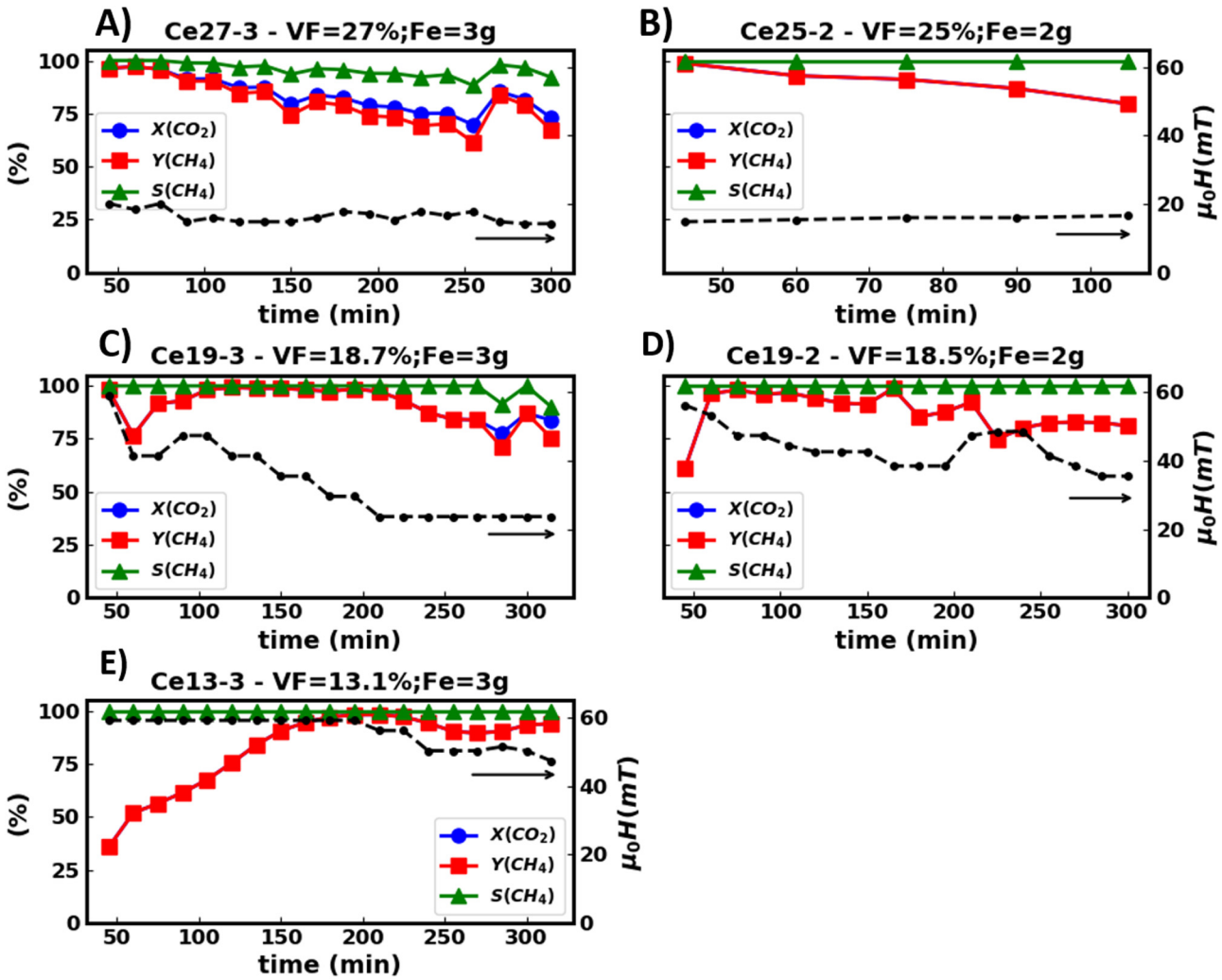

FIG. 8. Catalytic performance (plain lines) and applied magnetic field $\mu_0 H$ (black dash-dotted line) vs time for different iron volume fractions and masses of SiC-free catalysts. Whenever the selectivity $S(CH_4)$ is total, the conversion $X(CO_2)$ and the yield $Y(CH_4)$ overlap.

(32 mT) and low frequency (100 kHz), which is advantageous in terms of energy consumption. Indeed, the average power consumed by the oven during steady state regime ($T = 330\,°C$) was 360 W. By comparison, the air-cooled coil used under the best conditions with constant conversion ratio consumed an average power of 70 W ($\mu_0 H < 25$ mT). These conditions were reached in almost all previously presented experiments [Figs. 8(a)–8(c)] except sample Ce13-3 which contains 3 g of iron at a low volume fraction which required a high magnetic field to maintain its temperature and therefore more energy (450 W). Overall, this result demonstrates that magnetic heating is highly advantageous in terms of energy consumption providing an appropriate combination of heating agent mass and volume fraction.

VI. SYSTEM ENERGY PERFORMANCE

There are several ways to define energy performance, which depends on the final application. For a power-to-gas application, the relevant quantity is the ratio between the energy stored into the CH_4 molecules leaving the reactor and the input energy provided to the setup in the form of the electrical power (including the coil cooling system) and of the energy stored into the H_2 molecules. The superior calorific power (SCP) includes the variation of enthalpy of the reaction. These considerations explain the form of Eq. (1),

$$\eta = \frac{\mathrm{P(CH_4)}}{P(H_2) + P_{Coil}}, \tag{3}$$

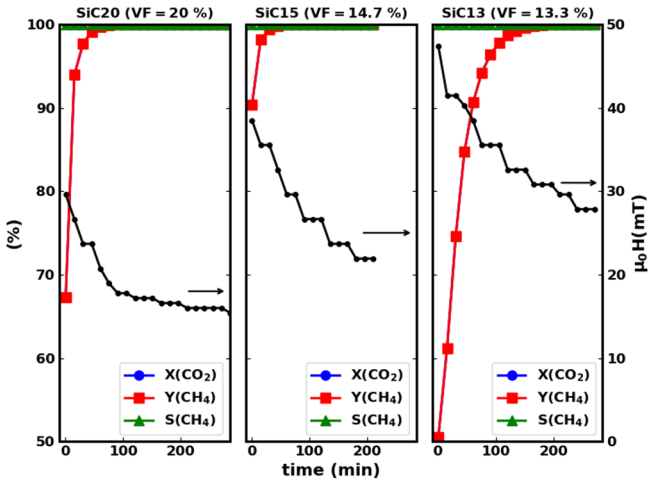

FIG. 9. Catalytic results as a function of time and applied magnetic field $\mu_0 H$ of samples SiC20, SiC15, and SiC13 [iron mass m(Fe) = 2 g]. Since the selectivity is total, $X(CO_2)$ and $Y(CH_4)$ overlap.

with $P(H_2)$ and $P(CH_4)$ being the power carried by the H_2 and CH_4 flows, respectively. The power carried by a given species X is given by the product of the gas flow $D_M(X)$ (mg min^{-1}) with the SCP, which represents the amount of energy generated by burning 1 mg of these gases,

$$P(X) = D_M(X) \times \mathrm{SCP}(X). \tag{4}$$

CO_2 gas has no SCP since it cannot be burnt. The experimental conditions considered for the energy efficiency calculation, the gas flow characteristics, and the energy efficiency of the Sabatier reaction are summarized in Table SI 1, Table SI 2, and Table SI 3 in the supplementary material, respectively. The coil's power consumption is given by a wattmeter.

The maximum theoretical efficiency (83%) is obtained when no extra heat is used for the reaction, i.e., when $P_{\mathrm{Coil}} = 0$ W. It is clear that decreasing the coil's power and maximizing the conversion of magnetic power into heat are key factors to reach high efficiency (see Fig. 11). By adjusting the Fe concentration in SiC-containing beds, it was possible to perform CO_2 methanation with low magnetic field power ($\mu_0 H \leq$ 30 mT) and to keep the catalytic performance. With a total flow rate of 25 ml min^{-1} (0.3 l h^{-1}) and $P_{\mathrm{Coil}} = 70$ W in the best conditions, the efficiency is $\eta \approx 4\%$, as shown by a red square in Fig. 11. Previous works published by our group,[17] using a 300 kHz water-cooled coil ($\mu_0 H = 28$ mT, $P_{\mathrm{Coil}} = 1800$ W) containing high SAR FeC nanoparticles as heating agent deposited on SIRAlOX® particles, with a flow of reactants of 125 ml min^{-1} and a methane yield $Y(CH_4) = 93.7\%$, obtained a total efficiency of $\eta \approx 0.7\%$. The improvement presented in this work is mainly due to the air-cooled coil, designed to operate at 100 kHz, which strongly decreases electric power consumption. The possibility to heat the magnetic particles with a low field intensity is also responsible for the low power consumption. Increasing the total flow rate to the maximum capacity of our setup, namely, 125 ml min^{-1} (1.5 l h^{-1}), and assuming ideally no loss in CH_4 selectivity, would lead to an efficiency of $\eta \approx 17\%$. This result could be improved even more by using the total volume of the coil; the maximum bed height was 3.8 cm, whereas the coil height is 20 cm, five times higher. According to Fig. 11, we can also see that reducing the coil power is expected to have a strong impact on the efficiency for medium flow rates (in the range 1 l h^{-1} to 10 l h^{-1}). The lower the coil consumption the higher is the gain in efficiency. It is also important to notice that decreasing the coil consumption power, keeping all the other parameters unchanged, has a marginal impact on the efficiency for large flow

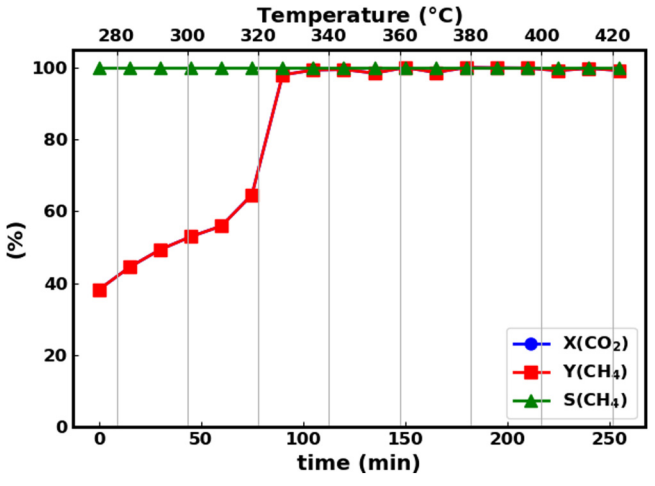

FIG. 10. Catalytic performance as a function of time in oven. The corresponding temperature of the catalytic bed is given on the top axis.

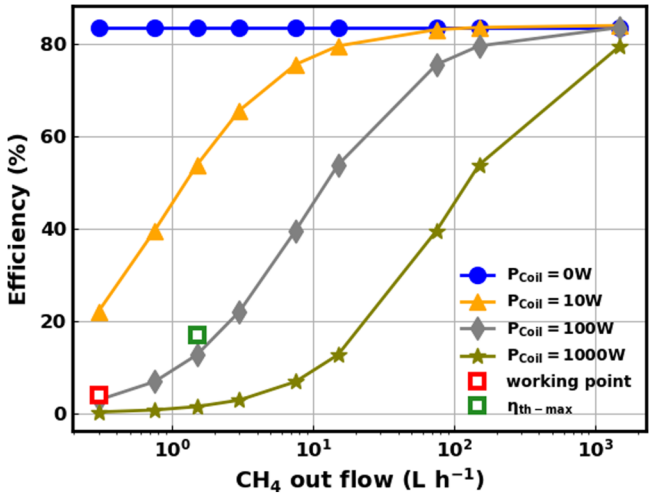

FIG. 11. Sabatier reaction efficiency calculated from Eq. (2) as a function of CH_4 outflow (with 100% yield) for different input coil's power. The current working efficiency (flow = 0.3 l h^{-1}, P_{coil} = 70 W, red square) and the maximum theoretical efficiency of our setup (green square) are also indicated.

rate ($\geq$1500 L h^{-1}). This result is encouraging for further developments of this technique.

VII. CONCLUSIONS

We show that CO_2 methanation can be carried out efficiently using Ni/CeO_2 as the catalyst and Fe powder as a heating agent in the presence of a 100 kHz alternating magnetic field. A thermal treatment under the magnetic field at the beginning of the catalytic reaction strongly increases the heating properties of the iron powder. It is demonstrated that a large part of this increase is due to the presence of eddy currents, which come as a complement to the hysteresis losses as heat source. This thermal treatment leads to the agglomeration of Fe microspheres into a block, which degrades the Ni catalytic activity. By controlling the Fe volume fraction and by adding SiC particles to the bed, this phenomenon is avoided and the catalytic performance and catalyst stability of the system are preserved. We propose that the diffusion mechanisms that determine the structural evolution of the Fe particles are determined by the bimodal size distribution of the catalytic bed. The structural morphology of the Fe microspheres drives, in turn, the formation of eddy currents and the efficiency of the magnetic-to-heat energy transfer. Future investigations would include, additionally, the volume fraction and the control of the particle size ratio to optimize the heat generation. Finally, the energy efficiency of the process has been improved compared to previous works, and the use of an air-cooled Litz wire coil being the major ingredient at the origin of this improvement. Basic calculations show that for the low gas flow, the coil's power consumption strongly limits the total efficiency of the process. However, this limitation might be less problematic for high flow rates. The improvement of the coil design and the increase of the gas flow rate should, in principle, increase the efficiency further, making induction heating a promising method for industrial applications of CO_2 hydrogenation.

SUPPLEMENTARY MATERIAL

See the supplementary material for the experimental setup and the detailed synthesis of the nanoparticles.

ACKNOWLEDGMENTS

The authors acknowledge the ERC Advanced Grant (MONACAT No. 2015-694159) and program HYDROMET (Région Occitanie) for financial support. The authors declare no competing financial interest.

DATA AVAILABILITY

The data and unavailable thesis reference that support the findings of this study are available from the corresponding author upon reasonable request.

REFERENCES

[1]S. Schiebahn, T. Grube, M. Robinius, V. Tietze, B. Kumar, and D. Stolten, Int. J. Hydrogen Energy **40**, 4285 (2015).
[2]G. Centi, E. A. Quadrelli, and S. Perathoner, Energy Environ. Sci. **6**, 1711 (2013).
[3]J. Gao, Q. Liu, F. Gu, B. Liu, Z. Zhong, and F. Su, RSC Adv. **5**, 22759 (2015).
[4]W. Wei and G. Jinlong, Front. Chem. Sci. Eng. **5**, 2 (2011).
[5]W. Wang, S. Wang, X. Ma, and J. Gong, Chem. Soc. Rev. **40**, 3703 (2011).
[6]L. Xu, F. Wang, M. Chen, J. Zhang, K. Yuan, L. Wang, K. Wu, G. Xu, and W. Chen, RSC Adv. **6**, 28489 (2016).
[7]S. Fujita, M. Nakamura, T. Doi, and N. Takezawa, Appl. Catal. A **104**, 87 (1993).
[8]H. C. Wu, Y. C. Chang, J. H. Wu, J. H. Lin, I. K. Lin, and C. S. Chen, Catal. Sci. Technol. **5**, 4154 (2015).
[9]M. Y. S. Hamid, M. L. Firmansyah, S. Triwahyono, A. A. Jalil, R. R. Mukti, E. Febriyanti, V. Suendo, H. D. Setiabudi, M. Mohamed, and W. Nabgan, Appl. Catal. A **532**, 86 (2017).
[10]S. Tada, T. Shimizu, H. Kameyama, T. Haneda, and R. Kikuchi, Int. J. Hydrogen Energy **37**, 5527 (2012).
[11]G. Zhou, H. Liu, K. Cui, A. Jia, G. Hu, Z. Jiao, Y. Liu, and X. Zhang, Appl. Surf. Sci. **383**, 248 (2016).
[12]L. Atzori, M. G. Cutrufello, D. Meloni, C. Cannas, D. Gazzoli, R. Monaci, M. F. Sini, and E. Rombi, Catal. Today **299**, 183 (2018).
[13]D. Türks, H. Mena, U. Armbruster, and A. Martin, Catalysts **7**, 152 (2017).
[14]M. Guo and G. Lu, RSC Adv. **4**, 58171 (2014).
[15]A. Sharma, I. Saito, H. Nakagawa, and K. Miura, Fuel **86**, 915 (2007).
[16]A. Meffre, B. Mehdaoui, V. Connord, J. Carrey, P. F. Fazzini, S. Lachaize, M. Respaud, and B. Chaudret, Nano Lett. **15**, 3241 (2015).
[17]A. Bordet, L.-M. Lacroix, P.-F. Fazzini, J. Carrey, K. Soulantica, and B. Chaudret, Angew. Chem. Int. Ed. **55**, 15894 (2016).
[18]S. Ceylan, C. Friese, C. Lammel, K. Mazac, and A. Kirschning, Angew. Chem. Int. Ed. **47**, 8950 (2008).
[19]S. Ceylan, L. Coutable, J. Wegner, and A. Kirschning, Chem. Eur. J. **17**, 1884 (2011).
[20]J. Hartwig, Angew. Chem. Int. Ed. **52**, 9813 (2013).
[21]S. S. Kale, J. M. Asensio, M. Estrader, M. Werner, A. Bordet, D. Yi, J. Marbaix, P.-F. Fazzini, K. Soulantica, and B. Chaudret, Catal. Sci. Technol. **9**, 2601 (2019).
[22]W. Wang, C. Duong-Viet, Z. Xu, H. Ba, G. Tuci, G. Giambastiani, Y. Liu, T. Truong-Huu, J.-M. Nhut, and C. Pham-Huu, Catal. Today **357**, 214–220 (2019).
[23]J. M. Asensio, J. Marbaix, N. Mille, L.-M. Lacroix, K. Soulantica, P.-F. Fazzini, J. Carrey, and B. Chaudret, Nanoscale **11**, 5402 (2019).
[24]P. M. Mortensen, J. S. Engbæk, S. B. Vendelbo, M. F. Hansen, and M. Østberg, Ind. Eng. Chem. Res. **56**, 14006 (2017).
[25]F. Varsano, M. Bellusci, A. La Barbera, M. Petrecca, M. Albino, and C. Sangregorio, Int. J. Hydrogen Energy **44**, 21037 (2019).
[26]M. R. Almind, S. B. Vendelbo, M. F. Hansen, M. G. Vinum, C. Frandsen, P. M. Mortensen, and J. S. Engbæk, Catal. Today **342**, 13 (2020).
[27]B. Mehdaoui, R. P. Tan, A. Meffre, J. Carrey, S. Lachaize, B. Chaudret, and M. Respaud, Phys. Rev. B **87**, 174419 (2013).
[28]K. Chang, H. Zhang, M. Cheng, and Q. Lu, ACS Catal. **10**, 613 (2020).
[29]R. R. Wildeboer, P. Southern, and Q. A. Pankhurst, J. Phys. D: Appl. Phys. **47**, 495003 (2014).
[30]V. Connord, B. Mehdaoui, R. P. Tan, J. Carrey, and M. Respaud, Rev. Sci. Instrum. **85**, 093904 (2014).